

Calibrated Quantitative Stroboscopic Schlieren Imaging of Ultrasound in Air

Eetu Lampsijärvi
Department of Physics
University of Helsinki
Helsinki, Finland
eetu.lampsijarvi@helsinki.fi

Jesse Heikkilä
Department of Physics
University of Helsinki
Helsinki, Finland
jesse.t.heikkila@helsinki.fi

Ivan Kassamakov
Department of Physics
University of Helsinki
Helsinki, Finland
ivan.kassamakov@helsinki.fi

Ari Salmi
Department of Physics
University of Helsinki
Helsinki, Finland
ari.salmi@helsinki.fi

Edward Hæggström
Department of Physics
University of Helsinki
Helsinki, Finland
edward.haeggstrom@helsinki.fi

Abstract—Ultrasonic bursts from two transducers were stroboscopically imaged with a Schlieren setup. A standard optical lens was used to calibrate the Schlieren images. The inverse Abel transform was used to gain the radial pressure distribution at each point when axial symmetry could be said to apply. Advantages and limitations of the technique are discussed.

Keywords—ultrasound, schlieren, quantitative, calibrated, stroboscopic

I. INTRODUCTION

There are few reported attempts to quantitatively visualize ultrasound (US) in air [1, 2] except for shockwaves. Conventional Schlieren imaging can't detect ultrasound waveforms in transparent media except in situations with standing waves. High-speed photography techniques paired with Schlieren methods exist [3], and as such enable photography of ultrasound, but calibrating the observations to absolute pressure units, using only conventional cameras to produce video material of airborne ultrasound has not been done before. We previously captured images of ultrasound in air [4], and the present work outlines calibration of such images of US bursts in air quantitatively, and with calibration of the perturbed pressure to Pascals. Caveats and applicability of the method are discussed.

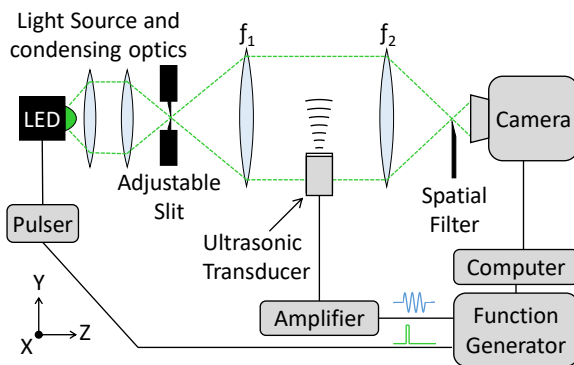


Fig. 1. Schematic illustration of the Schlieren arrangement.

II. METHODS

A. Schlieren experimental arrangement

A straight dual lens Schlieren system (Fig. 1) ($f_1 = f_2 = 200$ mm, $\phi = 24.5$ mm) was built to produce and image ultrasonic bursts. An LED (523nm, LZ1-00G102, LedEngin) was used as a strobe with a pulser [5], driven by a function generator (AFG 3252, Tektronix), which also fed the amplifier (AR 500A100A, Amplifier Research, PA, USA) driving the 200 kHz or 300 kHz ultrasonic transducers (MCUSD-19A-200B11RS & MCUSD-13A-300B09RS, Multicomp / Premier Farnell, UK). A digital camera (UI-3480CP, IDS Imaging, Germany) was used with an $f = 50$ mm lens ($\phi = 24.5$ mm) to capture images of a 33 by 25 mm² area. The adjustable slit was used to crop the light source to a 5.0 x 0.5 mm² rectangle. A microtome blade mounted on a three-axis translation stage was used as the spatial filter. The blade was adjusted to be parallel to the long edge of the image of the light source, to block half of the light, i.e. 50% cutoff to provide an even measuring range in both directions. The components were secured to an optical table with standard ThorLabs mounting supplies.

Short light pulses (nominally 100 ns, measured to be FWHM 450 ns) were produced in synchronization with US bursts while exposing each image. The propagation of the US burst could be studied by varying the delay (0 to 250 μ s) between the ultrasonic burst and the light pulse. As the US bursts are repeatable, the exposure time for each image could be set freely to achieve a balance between maximizing the signal to noise ratio (SNR) and minimizing the measurement time in a long series. Background images were collected after each image of an US burst, by imaging with the same parameters but having the US turned off. The ambient temperature, relative humidity, and pressure were monitored with BME280 (Bosch Sensortec, Germany) combination sensors and Pt100 platinum sensors to enable theoretical calculations for comparison. The image acquisition and function generator control were automated with a custom Python script.

B. Ultrasonic driving parameters

Five cycles of sine wave (202730 Hz & 301980 Hz, 400 Vpp) were used to drive the US transducers. A slow pulse repetition frequency (PRF) of 125 Hz was used to minimize heating of the US transducers while maximizing the number of bursts per time. The voltage applied to the transducer was measured with a 100x probe and an oscilloscope, and the source voltage at the function generator was adjusted until the target voltage of 400 Vpp at the transducer was reached. The driving frequencies were selected based on impedance measurements (Impedance Analyzer for Analog Discovery, Digilent Inc., WA, USA) of the transducers. The selected driving voltage was the maximum input voltage specified on the data sheet of the 300 kHz transducer.

C. Calibration procedure

A weak positive lens ($f = 10 \text{ m} \pm 2\%$ at 543 nm, $\sigma = 25.4 \text{ mm}$, 110-0295E, Eksma Optics, Lithuania) was used as a standard to calibrate the Schlieren images. Using standard objects to calibrate Schlieren images are now outlined briefly; a more detailed account is given in [3] and a practical example in [6]. As the optical properties of positive weak lenses are well known, each pixel on an image of a standard lens can be linked to the refracted angle, ϵ , of a ray of light passing through that location on the lens (Fig. 2.). Pixels with the same intensity in the actual Schlieren image imply the same refracted angle. Background subtraction is used to negate the effects of slight unevenness of the Schlieren background and debris on the sensor. The light absorption of the standard lens was measured by comparing the mean intensity over the lens area against the background intensity, when no Schlieren cutoff was applied i.e. using conventional photography. The transmittance of the lens was found out to be 91.3%, which was accounted for when acquiring the calibration curve.

The refracted angle data can be integrated along the optical axis to gain the refractive gradient index as shown in [6]. For this, a characteristic length scale and a constant refractive index

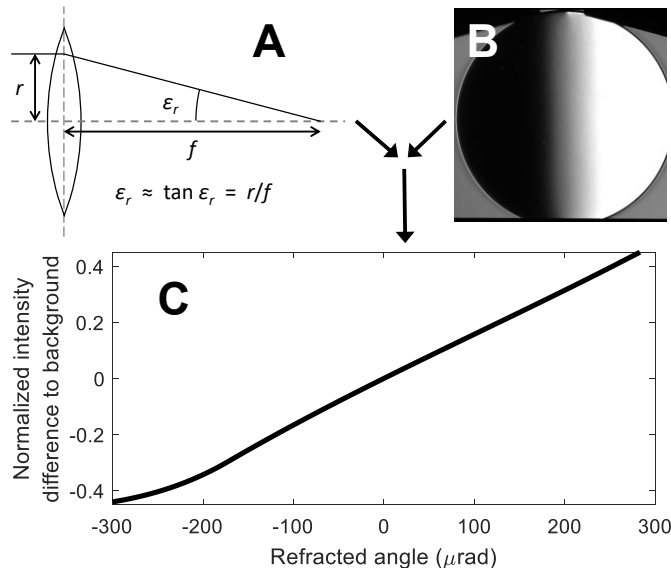


Fig. 2. A: Optical principle behind the calibration. B: positive lens used as a Schlieren standard object to link pixel intensity to refracted angle, ϵ . C: Resultant calibration curve. One unit is the full 12-bit range of the camera

gradient along the optical axis (Z) needs to be assumed, which makes the approach ill-suited for axially symmetric or irregular phenomena. In axially symmetric phenomena, the inverse Abel transform that corresponds to the inverse Radon transform for axially symmetric cases, may be used to obtain the refractive index gradient in cylindrically symmetric cases. In cases where approximating the phenomenon as axially symmetric or rectangular are out of the question, tomographic methods need to be used.

$$f(r) = -\frac{1}{\pi} \int_r^\infty \frac{dF(x)}{dx} \frac{1}{\sqrt{x^2 - r^2}} dx \quad (1)$$

In practice, the inverse Abel transform (1) is performed numerically to obtain the radial distribution $f(r)$ from the corresponding projection $F(x)$. In the present work, $F(x)$ is the refracted angle data obtained from the calibrated Schlieren images, and $f(r)$ is the change in refractive index, dn/dx , as a function of radial distance from the axis of symmetry. The pyAbel Python library [7] was used to perform the inverse Abel transforms using the BASEX method [8]. The inversion is sensitive to noise, thus 2D median and Gaussian filtering is used with small kernels, as not to affect the shape of the wavefronts too much. MATLAB R2019a (MathWorks, MA, USA) was used for all other image processing. The length scale of the images was calibrated by imaging a grid of known length scale.

Once the radial distribution of refractive index gradient has been calculated, the refractive index itself can be found by integrating along the axis of Schlieren sensitivity, which in this case is the X-axis. The integration constant is of no consequence as long as the integration starts from an area of the image which has been undisturbed by the phenomenon. This holds true as we are interested in the perturbed pressure instead of the absolute pressure. The Gladstone-Dale relationship can be rearranged (2) to calculate the density, ρ , from the refractive index:

$$\rho = (n - 1)/\kappa \quad (2)$$

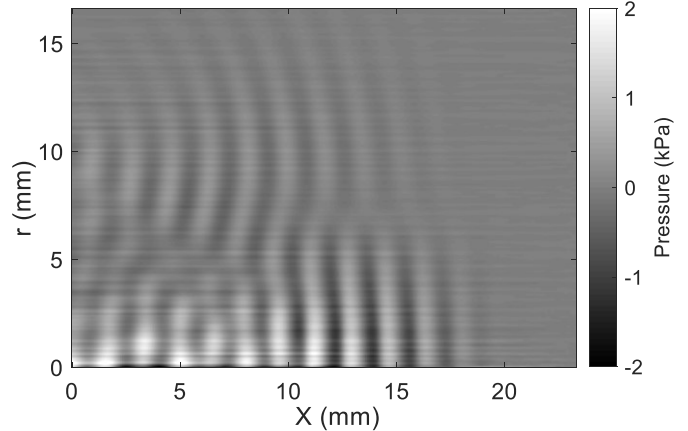


Fig. 3. Pressure field emitted by the 200 kHz transducer as a function of radial and X-distance. X = 0 is set at 0.3mm right from the transducer surface. The transducer has a radius of 9 mm. The burst propagates from left to right. Filtering is required to suppress the centerline noise caused by the inverse Abel transform. Gaussian filtering with a standard deviation of 2.5 pixels (less than $\lambda/50$) was applied before the Abel inversion, and a median filter with a 0.14mm length was applied along the radial direction before integration in the X direction. The data presented is an average across 2640 US bursts and light pulses.

Here n is the refractive index, and κ is the Gladstone-Dale constant. The pressure can be obtained via an equation of state, or by (3) linking the perturbed density ρ' to the perturbed pressure p' via ambient sound velocity c_0 .

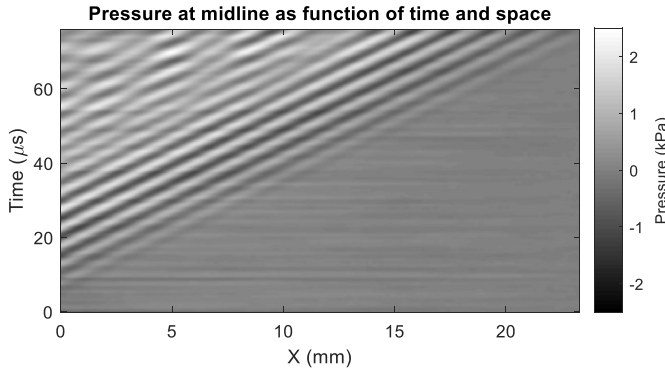


Fig. 4. Flow of the US burst through the imaged area.

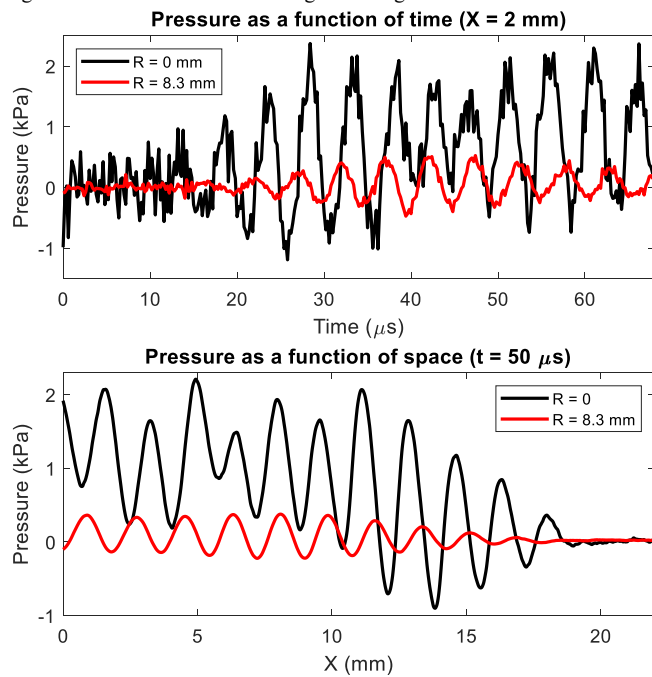


Fig. 5. Details extracted from the data present in Fig. 4 with the corresponding details at a different radial distance. The data at $r = 0$ suffers from centerline noise affecting the integration. The pressure field at $r = 8.3$ mm is free from most interference effects and has higher SNR.

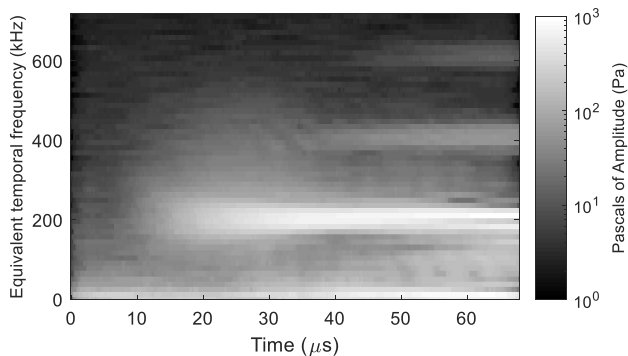


Fig. 6. Spatial frequency content at the midline, i.e. the acoustic axis, as a function of time. Time points after the US burst starts to leave the imaging area have been excluded.

$$p' = \rho' c_0^2 \left(1 + \frac{1}{2} \frac{B}{A} \frac{\rho'}{\rho} \right) \quad (3)$$

B/A in (3) is the nonlinearity parameter, which is 0.4 for air [9], and (3) is a one-step improvement from using the ideal gas law to acquire the pressure, especially as the ambient sound velocity can be deciphered from the Schlieren images themselves, and the waveform shape suggests slight nonlinear effects being present.

III. RESULTS

The pressure distribution emitted by the 200 kHz transducer as a function of axial distance from the transducer (X) and radial position is presented in Fig. 3 at $t = 60 \mu\text{s}$. The US burst is characterized by an amplitude of 1 kPa that grows smaller with distance from the transducer. Nearfield interference patterns are observed near the transducer. The progression of the wave in time along the midline i.e. at $r = 0$, is seen in Fig. 4. Interference effects are observed starting from $40 \mu\text{s}$. The sound velocity can be extracted from Fig. 4 and confirmed to match with theoretical prediction (at 22.6 C, 54% relative humidity). Data beyond $68 \mu\text{s}$ is riddled with artefacts due to the US burst exiting the imaged area and invalidating the assumption of the right edge being at ambient pressure.

Fig. 5 shows two line profiles, one in time and one in the spatial domain, from Fig. 4 for clarity. Fig. 5 also shows two lines extracted at $r = 8.3$ mm instead of at the centerline, i.e. acoustic axis, to exemplify how the centerline noise, and thus the error in the integral, is lower away from the centerline. The SNR is higher in the spatial dimension. Tighter sampling in time and temporal filters would be possible at the expense of increased measurement time.

Fig. 6 displays a spectrogram of spatial frequency content in the X -direction at $r = 0$ at each time point of Fig. 4 up to $68 \mu\text{s}$. The first $10 \mu\text{s}$ are rather silent as the US burst has yet to fully emerge from the transducer. As the burst emerges, the frequency content is centered around 200 kHz as expected. After the burst has propagated for 30 to $40 \mu\text{s}$, one perceives generation of harmonics. A low frequency component is present, which is mainly a contribution of centerline noise causing errors to the integration.

Fig. 7 shows how Schlieren images of the US burst emitted by the 300 kHz transducer were obtained, but due to the asymmetric nature of the near field, use of the Abel inversion could not be justified, and further processing was abandoned. Tomographic methods could be used to circumvent the issue.

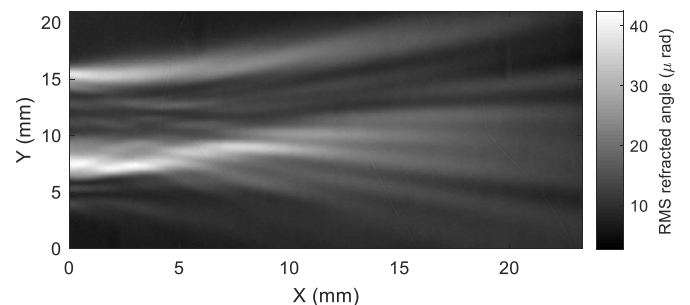


Fig. 7. Calculated RMS (over $160 \mu\text{s}$) of the refracted angle for images of the burst emitted from the 300 kHz transducer. The near field is asymmetric.

IV. DISCUSSION

The caveats of the method are known as it has been used extensively for flow visualization studies [3, 10]. The main limitation of the method presented in this work is the requirement for axial symmetry in the imaged phenomena. As exhibited by the unexpected asymmetry in Fig. 7, one should not blindly apply the assumption of axial symmetry. Luckily any severe asymmetry will be obvious from a quick inspection of the raw data. To overcome this limitation, including a motorized rotational stage in the system would facilitate the collection of tomographic projections, i.e. allowing automated rotation of the transducer, and with it the US burst.

Centerline noise is problematic, especially when studying phenomena near the inversion axis. The problem is exacerbated if absolute or RMS values are used, see Fig. 8, where the RMS noise floor exceeds the studied signal. If some properties of the signal under study may be assumed, high pass filtering may be used to remove most of the unwanted effects caused by centerline noise in cases like Fig. 5. If the exact fine structure of the US field is of no concern, a straightforward assumption of a characteristic length scale at the midline may yield adequate results, if the phenomenon under study is nearly planar. As for adequacy, for the presented 200 kHz transducer with a diameter of 19 mm, an error of 1 mm in the assumed length scale would result in 5% of additional error. Measuring the refractive index gradient in both the x and y directions would allow setting a reference point of pressure instead of having to assume a known pressure for every line integrated. This should alleviate problems related to small errors in the measured gradient, which lead to the horizontal artefacts visible in Fig. 3 and Fig. 4.

The method of calibrating against an optical standard is well known [3, 11]. The main drawbacks relate to post processing rather than to the calibration itself, but [10] points out that the interference fringes around the edges of opaque objects do not follow the same pixel intensity to angle relationship as pixels in areas far away from edges. Background subtraction should alleviate this problem, but the solution offered by [10] is to generate calibration curves for every pixel by adjusting the Schlieren cutoff. The drawback is additional processing and that the calibration becomes valid only for one specific sample arrangement.

In the present work the lens standard is specified to 2% tolerance in focal length, which translates directly to uncertainty

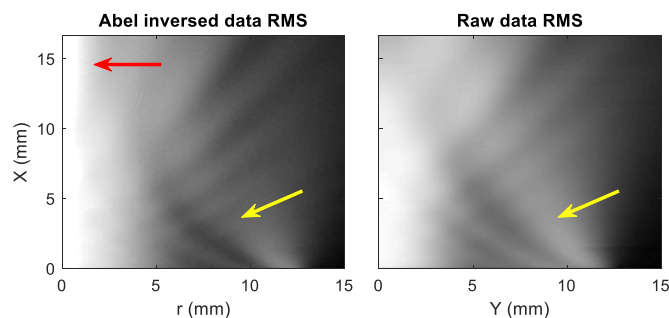


Fig. 8. Comparison of RMS pattern after the Abel inversion (left) and of the original projection data (right). The color scales are logarithmic. The Abel inversion reveals the fine structure in the near field better (approximate location pointed by yellow arrows), but suffers from artefactual centerline noise (red arrow). The vertical scale is identical in both images.

in the calibration curve. Correcting for the difference in the wavelength of the light used would yield a relative correction of 0.3 %. The Gladstone-Dale constant is constant over a wide range of temperatures, and the use of the Gladstone-Dale relationship instead of the Lorentz-Lorenz equation is justified for gases [12]. Monitoring the ambient temperature is important, unless the measurement series allows for accurate determination of the ambient sound velocity. Relative humidity and ambient pressure are minor factors [13], but need to be monitored if precise theoretical calculations are to be made for comparison.

We built a Schlieren system capable of stroboscopically imaging repeatable US bursts in air. We calibrated the system to yield deflected angles, from which the corresponding pressure distribution for axisymmetric bursts was obtained. The system is sensitive enough to detect 10 Pa changes in the imaged US burst (Fig. 5 & Fig. 6). The present results are to be compared to other calibration methods such as calibration by laser interferometry, although similar work exists [14].

REFERENCES

- [1] J. Bucaro, "Visualization of ultrasonic waves in air", *The Journal of the Acoustical Society of America*, vol. 62, no. 6, p. 1506, 1977. Available: 10.1121/1.381657.
- [2] J. Harvey, H. Smithson and C. Siviour, "Visualization of acoustic waves in air and subsequent audio recovery with a high-speed schlieren imaging system: Experimental and computational development of a schlieren microphone", *Optics and Lasers in Engineering*, vol. 107, pp. 182-193, 2018. Available: 10.1016/j.optlaseng.2018.03.015.
- [3] G. Settles, *Schlieren and shadowgraph techniques*. Springer, 2013.
- [4] E. Lampisjärvi, I. Kassamakov, and E. Hæggröm, "Stroboscopic time resolved Schlieren visualization of 220 kHz ultrasound in air," *Physics Days 2019*, Turku, Finland.
- [5] T. Paulin, V. Heikkinen, I. Kassamakov and E. Hæggröm, "LED driver for stroboscopic interferometry", *Optical Micro- and Nanometrology IV*, 2012. Available: 10.1117/12.922119
- [6] M. Hargather and G. Settles, "A comparison of three quantitative schlieren techniques", *Optics and Lasers in Engineering*, vol. 50, no. 1, pp. 8-17, 2012. Available: 10.1016/j.optlaseng.2011.05.012.
- [7] PyAbel 0.8.3 library, <https://dx.doi.org/10.5281/zenodo.594858> P. Ciddor, "Refractive index of air: new equations for the visible and near infrared", *Applied Optics*, vol. 35, no. 9, p. 1566, 1996. Available: 10.1364/ao.35.001566.
- [8] V. Dribinski, A. Ossadtchi, V. A. Mandelshtam, and H. Reisler, "Reconstruction of Abel-transformable images: The Gaussian basis-set expansion Abel transform method," *Review of Scientific Instruments*, vol. 73, no. 7, pp. 2634-2642, 2002.
- [9] M. Hamilton and D. Blackstock, *Nonlinear acoustics*. Melville, NY: Acoustical Society of America, 2008.
- [10] B. Hannah, "Quantitative schlieren measurements of boundary layer phenomena", in *Proc. 11th Intl. Congr. on High Speed Photography*, 1975, pp. 539-545.
- [11] H. Schardin, "Das Toeplersche Schlierenverfahren: Grundlagen für seine Anwendung und quantitative Auswertung", *VDI-Forschungsheft No. 367, 5(4)*, pp. 1-32, 1934.
- [12] L. Vasil'ev, *Schlieren methods*. New York: Israel Program for Scientific Translations, 1971.
- [13] O. Cramer, "The variation of the specific heat ratio and the speed of sound in air with temperature, pressure, humidity, and CO2 concentration", *The Journal of the Acoustical Society of America*, vol. 93, no. 5, pp. 2510-2516, 1993. Available: 10.1121/1.405827.
- [14] R. F. Bell and L. Fottner, "Schlieren method with Quantitative Evaluation by Digital Image Processing", in *Proc. 12th Symposium on Measuring Techniques for Transonic and Supersonic Flows in Cascades and Turbomachines*, Prague, 1994.